Author(s): Islam, Md. Mazidul & Rasilainen, Kimmo & Viikari, Ville

Title: Implementation of Sensor RFID: Carrying Sensor Information in the Modulation Frequency

Year: 2015

Version: Post print

Please cite the original version:

Islam, Md. Mazidul & Rasilainen, Kimmo & Viikari, Ville. 2015. Implementation of Sensor RFID: Carrying Sensor Information in the Modulation Frequency. IEEE Transactions on Microwave Theory and Techniques. Volume 63, Issue 8. 2672-2681. ISSN 0018-9480 (printed). DOI: 10.1109/tmtt.2015.2446476.

Implementation of Sensor RFID: Carrying Sensor Information in the Modulation Frequency

Md. Mazidul Islam, Kimmo Rasilainen, and Ville Viikari, *Senior Member, IEEE*

***Abstract*—An approach that can be used for exploiting the sensing capabilities of radio-frequency identification (RFID) is presented and formulated. In this approach, sensor information is carried through the modulation frequency of RFID . The aim of this work is to investigate the sensor concept and to characterize the sensor performance both theoretically and experimentally. Furthermore, the operation of the sensor radio-frequency (RF) parts and oscillator are described analytically, and the equations are verified by simulations and measurements. The concept is experimentally demonstrated at a single carrier frequency to test its suitability for ultra-high frequency (UHF) RFID applications, and shown to be feasible for implementing sensors that can be read across distances up to 14 meters.**

***Index Terms*—Diode, mixer, modulation, oscillator, radio frequency identification (RFID), rectifier, wireless sensors.**

I. Introduction

ULTRA-high frequency (UHF) and microwave radio-frequency Identification (RFID) enables identifying distant objects equipped with an RFID tag [1]. The technology has become increasingly ubiquitous, including applications such as asset tracking and inventory in logistics, access control, and road toll collection. In addition to existing applications, there is a huge need for an inexpensive technology capable of both identification and of sensing some external parameter, such as pressure, temperature or strain. Battery-powered active or semi-passive wireless sensors are often available, but they may be too expensive or bulky for many applications. In addition, their life-time or environmental operating conditions can be limited by the battery. These limitations can be avoided by using passive wireless sensors.

Communication methods used by passive wireless sensors can be divided into analog and digital ones. Digital sensors are also known as RFID and can further be divided into two sub-categories, depending on whether the sensor read-out is analog or digital [2].

RFID tags equipped with integrated circuits (IC) enable several sophisticated features such as identification, rewritable memory and anti-collision protocol. UHF RFID has been used for sensing by adding an A/D converter, a microprocessor or other digital logic and a sensing element to the tag [3]−[9]. In this digital sensing approach, an analog sensor value is transformed into digital format and communicated to the reader device using the digitally modulated backscattering principle. The advantage of this approach is that it facilitates a generic sensor element and is thus well suited for a very broad range of applications. However, increased power consumption due to the additional electronics reduces the read-out range significantly. As an example, sensors presented in [9] provide a read-out range of 1.5 m while RFID tags without a digital sensor provide a range in the order of 15 m. Therefore, a long read-out distance of UHF RFID sensor tags necessitates an on-board battery or other energy source.

Examples of RFIDs equipped with analog sensors are presented in [10]−[14]. In this approach, the RFID antenna impedance (and thus the matching frequency) is made sensitive to a measured quantity, such as moisture, by loading the antenna with a moisture-sensitive element. The sensed quantity can be obtained in two ways. In one, the reader interrogates the sensor at different frequencies and records either relative sensitivity or modulated radar cross-section of the tag as a function of frequency. The sensed quantity can be related to these responses through antenna matching. The second way of obtaining the sensed quantity is to add a tuning circuit to the RFID chip. This tuning circuit is used to find the input impedance that maximizes the power transfer between the reader and the tag.

The advantage of using the antenna as a sensor is a relatively long read-out distance because the sensing element does not necessarily increase the power consumption. However, the concept requires a sensing element operating at microwave frequencies. Typical off-the-shelf sensors are not feasible because they are often designed to operate at frequencies below a few MHz. Furthermore, the antenna impedance also changes due to proximity to conductive or dielectric objects, which can falsify the sensor read-out [15].

Sensors utilizing analog communication are surface acoustic wave (SAW) RFID, intermodulation sensors and resonance sensors. SAW sensors [16]−[18] utilize an interdigital transducer patterned on a piezoelectric substrate to convert the electromagnetic energy into a surface-acoustic wave, which is then manipulated with acoustic reflectors, transformed back to electromagnetic energy, and radiated back to the reader device. The measured quantity affects the propagation properties of the SAW on the piezoelectric substrate. The need for a piezoelectric material for the sensing element limits possible applications. In addition, SAW tags only enable hard-coded identification (ID).

Resonance sensors (e.g., [19]−[21]) consist of a simple resonance circuit whose resonance is sensitive to a measured quantity. These sensors require near-field coupling to the reader, which limits their read-out distance to a few centimeters. Another hindrance is that their resonance may

Manuscript received Feb. 9, 2015; This work was supported in part by the Academy of Finland under decisions 267420 and 289320, by the Metso Corporation, Finland, by the Aalto ELEC Doctoral School and by the Nokia Foundation.

The authors are with the Department of Radio Science and Engineering, Aalto University School of Electrical Engineering, FI-00076 Aalto, Finland (mazidul.islam@aalto.fi).

TABLE I
SUMMARY OF PASSIVE WIRELESS SENSORS

	Resonance sensor	SAW RFID	Intermod. sensor	RFID + sensitive antenna	RFID + digital sensor	This work
Communication	Analog	Analog	Analog	Digital	Digital	Digital
Sensing	Analog	Analog	Analog	Analog	Digital	Analog
ID	No	Yes	Yes	Yes	Yes	Yes
Memory	No	No	No	Yes	Yes	Yes
Anti-collision	No	No	No	Yes	Yes	Yes
Environment insensitive	No	Yes	Yes	No	Yes	Yes
Read-out distance	Small	Large	Large	Large	Small	Large
Sensing element	Generic	Special	Generic	Special	Generic	Generic
Reader device	Special	Special	Special	Standard	Standard	Standard

be affected by proximity to conductive or dielectric objects.

Recently developed intermodulation sensors utilize frequency conversion for sensor read-out [22] – [26]. In this principle, the sensor is interrogated by two closely located frequencies, and the sensor responds at an intermodulation frequency. This approach enables wireless read-out of a generic sensor element, such as a Microelectromechanical systems (MEMS) sensor across a very large distance (even tens of meters). The sensors can also be equipped with a hard-coded ID. Intermodulation sensors can be made insensitive to antenna proximity effects.

The properties of passive wireless sensors are summarized in Table I. No single technology can simultaneously provide identification, anti-collision protocol, memory, insensitivity to antenna proximity effects, and large interrogation distance. In this paper, we present a passive wireless sensor principle potentially capable of offering all these benefits. The sensor utilizes the digital communication principle of RFID, and the sensor information is coded into the digital modulation frequency of the backscattered signal. It complies with the frequency regulations set for UHF RFID in the ISO/IEC18000-6C standard and can be compatible with existing high-end readers capable of recording the modulation frequency of the tag with sufficient precision (e.g., Infinity 510 manufactured by Sirit or Tagformance Lite by Voyantic). Compatibility with some existing RFID hardware offers substantial cost benefits.

Previously, the idea of converting sensor information to the modulation frequency of a backscatter transponder has been presented in [27] – [29], but the concept is not analyzed in detail. Moreover, analytical equations for predicting the sensor performance have not been developed yet. Thus, the aim of the current work is to analyze the sensor principle and to develop analytical equations for predicting the sensor performance. In addition, equations for the sensor radio-frequency (RF) parts and oscillator are derived and demonstrated in practice. Finally, the analytically predicted sensor performance is compared with measurement results. Digital circuitry of RFID (such as memory, analog-to-digital converter, or envelope detector) is beyond the scope of the current work. However,

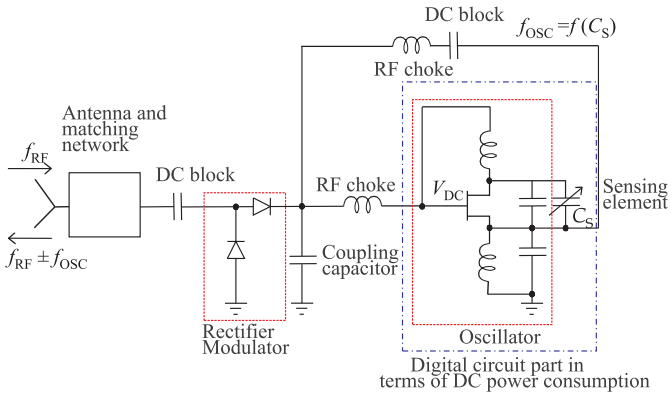

Fig. 1. Simplified RF circuit of the sensor.

the oscillator and sensing element described in this paper could replace the local oscillator in the digital circuitry of a conventional RFID tag. As a consequence, the remaining digital part would consume less power.

II. ANALYTICAL MODEL FOR THE SENSOR

A. Operation Principle of the Sensor

An RFID reader communicates with the tag using a binary amplitude modulation. The tag rectifies the required energy for its operation from the interrogation signal of the reader, and replies to the reader by reflecting a portion of the signal carrying a binary modulation back to the reader. The sensor proposed in this paper operates in a similar way as a normal UHF RFID tag, except that the modulation frequency of the tag carries sensor information. According to the ISO/IEC 18000-6C standard, the modulation frequency of the tag is set by the reader device at the beginning of the communication, and it can be from 40 kHz to 640 kHz [30]. The modulation frequency of the tag can vary $\pm 4...22\,\%$ from the initially set frequency depending on the frequency and operating conditions. This enables coding sensor information to the modulation frequency.

The sensor can be realized by modifying the internal oscillator of an RFID chip in such a way that its oscillation

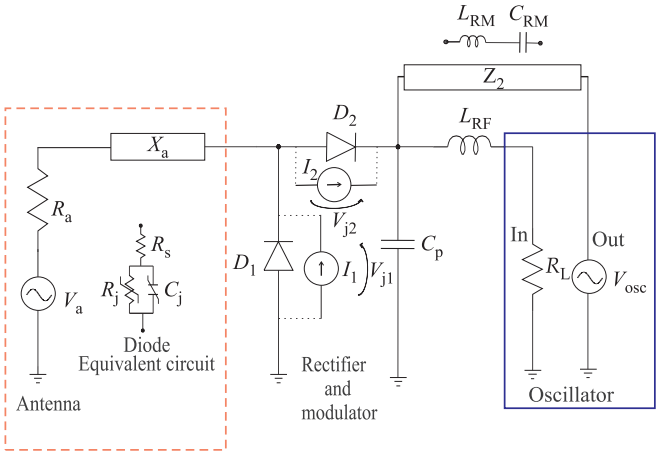

Fig. 2. Electrical equivalent circuit of the antenna, rectifier, and modulator. The oscillator is represented with a resistor at its dc input and an ac voltage source at its output.

frequency tunes with the measured quantity. This can be done by loading the oscillator with an inductive, capacitive or resistive sensor element. An advantage of this principle is that generic sensor elements, such as MEMS sensors, can be used because the sensor is read out at low kHz frequencies. The sensing element does not necessarily increase the power consumption of the tag, and the principle therefore offers a long read-out distance. The sensor circuitry is also fully isolated from the antenna, making the concept insensitive to antenna proximity effects. This concept can potentially be made compatible with the existing RFID systems, and many sensing elements can be incorporated into one RFID tag with digitally controlled switches. The sensing elements can be arranged so that the oscillation frequency is affected by only one element at a time [15].

The main RF parts of the sensor (excluding the antenna) are voltage rectifier, oscillator, and modulator. The rectifier produces dc voltage for the oscillator from the received interrogation signal. When the oscillator turns on, it produces an ac output, which drives the modulator. As a consequence, a modulated signal is scattered back. In the studied case, the rectifier and modulator are the same element. Fig. 1 shows a simplified RF circuit of the sensor. In the following, we present different parts of the sensor in more detail and derive analytical equations to describe their electrical behavior.

B. Voltage Rectifier

The rectifier is based on two Schottky diodes and a capacitor. This rectifier topology is also known as a voltage doubler [31]. A voltage doubler circuit is selected instead of a voltage quadrupler or $2N$-fold voltage multiplier because it is relatively simple to realize in practice with discrete components. The antenna is matched to the rectifier at the carrier frequency, and RF chokes are used to prevent RF signal from dissipating in the oscillator ports. A dc block capacitor (C_b) is placed between the diode and antenna to prevent rectified voltage from grounding through the antenna, and a coupling capacitor (C_p) is used to ground the RF signal. Fig. 2 shows the electrical equivalent circuit of the rectifier. Antenna and matching circuit with dc block capacitor are represented as a voltage source with an internal impedance of $Z_a = R_a + \jmath X_a$, and the dc load of the oscillator is R_L.

In the following, we derive an equation for the rectified dc voltage across the load R_L under small-signal conditions. The rectified voltage is later needed to predict the sensitivity of the sensor (i.e., the lowest RF power that turns the sensor on) and to predict the modulated radar cross-section of the sensor.

When the sensor is illuminated by the reader device, the antenna produces a voltage

$$V_a = 2\sqrt{2P_{in}R_a}\cos(\omega_0 t) \tag{1}$$

where P_{in} is the received power, R_a is the antenna resistance, and ω_0 is the angular frequency. Assume that dissipations in the series resistance R_s of the diodes are small compared to those in the junction resistance R_j. The Schottky diode is zero-biased (possible self-biasing is neglected for simplicity), and its junction resistance is given as $R_j = 1/(\alpha I_s)$ where I_s is the saturation current and $\alpha = q/nkT$ where q is the elementary charge, n is an ideality factor, k is the Boltzmann constant and T is temperature. Fig. 2 depicts that at the time of rectification, two diodes (D_1 and D_2) produce two different junction voltage V_{j1} and V_{j2}, respectively. For the sake of simplicity we calculate the rectifier dc voltage for each diode one at a time and sum the results later to obtain the total rectified dc voltage. In dc analysis, the junction capacitance can be neglected and the diode is represented as R_j. The junction voltage across diode 1 is

$$V_{j1} = 2\sqrt{2P_{in}R_a}S_{ja1}\cos(\omega_0 t) \tag{2}$$

where $S_{ja1} = V_{j1}/V_a$ is the voltage transfer function from the antenna to diode 1. The small-signal approximation for junction currents under zero bias is

$$I(V_j) \approx I_s + I_s\alpha V_j + \frac{(I_s\alpha^2)}{2}V_j^2. \tag{3}$$

The linear term of V_j represents the linear resistance and the square term of V_j contributes to rectification. Let us substitute (2) into the last term of (3). The dc current is

$$I_{1(j,DC)} = 2I_s\alpha^2 P_{in}R_a S_{ja1}^2. \tag{4}$$

This current can be represented by an equivalent current generator in parallel with the junction. The dc voltage produced by diode 1 across the load R_L (i.e., the supply voltage for the oscillator) can be expressed as

$$V_{1(DC)} = I_{1(j,DC)}\left(\frac{R_j R_L}{2R_j + R_L}\right). \tag{5}$$

Following the same procedure for diode 2 and adding the contribution from both diodes, the overall rectified dc voltage is given as

$$V_{DC} = \left(I_{1(j,DC)} + I_{2(j,DC)}\right)\left(\frac{R_j R_L}{2R_j + R_L}\right). \tag{6}$$

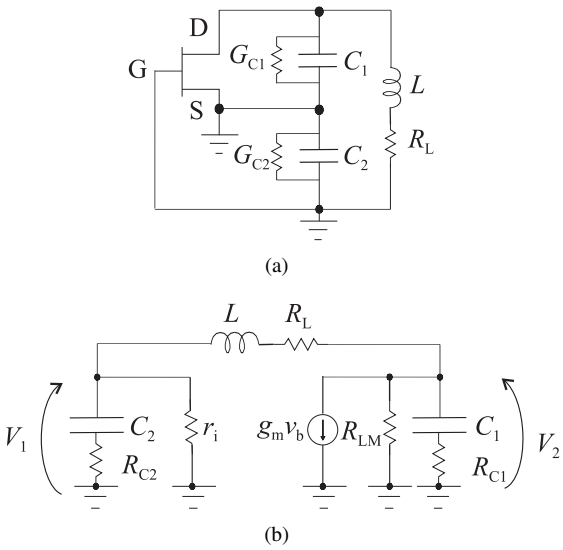

Fig. 3. (a) Colpitts oscillator circuit without bias network, (b) Small signal electrical equivalent circuit of Colpitts oscillator.

C. Oscillator

A Colpitts oscillator topology is selected because it is relatively simple to analyze and realize in practice with discrete components. However, other classical oscillator topologies could be used as well. Fig. 3(a) shows a Colpitts oscillator circuit without biasing network. In the proposed concept, sensing is realized in two ways: either replacing C_1 or C_2 with a capasitive sensor, or by connecting a capacitive sensitive element in parallel or in series with either of the capacitors. Possible losses of the sensing element can be embedded into G_{C1} or G_{C2}, depending on the chosen configuration.

Small-signal analysis is used to evaluate the startup condition and to calculate the oscillation frequency. Let us represent the Colpitts oscillator with the small-signal equivalent circuit shown in Fig. 3(b). In the following, we derive equations for the oscillation frequency, turn-on dc voltage, and output ac voltage.

1) Oscillation Frequency and Condition: The Kirchhoff equations for the two voltage nodes of the circuit in Fig. 3(b) can be expressed in matrix format as

$$[\mathrm{Y}]\,[\mathrm{V}] = 0$$

in which

$$[\mathrm{Y}] = \begin{bmatrix} j\omega C_2 + G_{C2} + G_i + Y_L & -Y_L \\ g_m - Y_L & j\omega C_1 + G_{C1} + Y_L + G_{R_{LM}} \end{bmatrix}$$

$$[\mathrm{V}] = \begin{bmatrix} V_1 \\ V_2 \end{bmatrix}$$

where $G_i = r_i^{-1}$ is the transistor input admittance, g_m is the transconductance; and G_{C1} and G_{C2} represent the conductance of capacitors C_1 and C_2 respectively. The feedback inductor admittance is $Y_L = (j\omega L_1 + G_{R_L})^{-1}$, $G_{R_{LM}} = R_{LM}^{-1}$, where R_{LM} is the load resistance. Oscillation is possible when the determinant of the admittance matrix equals zero. By requiring this condition, we get an equation for the oscillation frequency

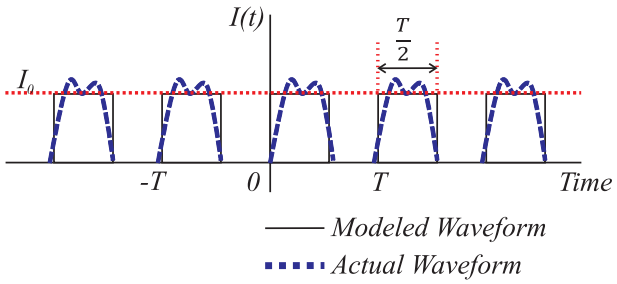

Fig. 4. Actual and modeled drain current waveform of the transistor [32].

$$f = \frac{1}{2\pi}\sqrt{\frac{G_i g_m G_{R_L} G_{R_{LM}} G_{C1} G_{C2}}{C_1C_2 + C_1L_1 + C_2L_1}} \tag{7}$$

and an equation for the oscillation condition

$$\left[\frac{C_1\left(G_i + G_{R_L} + G_{C2}\right) + C_2\left(G_{R_{LM}} + G_{R_L} + G_{C2}\right)}{\left(G_i + G_{R_{LM}} + g_m + G_{C1} + G_{C2}\right)}\right] \geq L_1. \tag{8}$$

2) Oscillator Output Voltage: In the oscillator circuit, a capacitive feedback is formed by capacitors C_1 and C_2. The output voltage of the oscillator is derived from the time-domain waveform of the drain current $I(t)$, as shown in Fig. 4. For output voltage calculation, the periodic drain current is modeled by a square wave with a period of $T_0 = 2\pi/\omega_0$ and amplitude I_0. The maximum drain current occurs when the gate voltage reaches its peak value.

Assuming that the amplitude of the output oscillating signal is A, the maximum drain current $I_1(t)$ can be approximated when the transistor operates in the nonsaturated region [32]

$$I_0 = \mu_n C_{ox}\frac{W}{L}\left[(V_{DC} + A + nA - V_t)(V_{DC} - A) - \frac{1}{2}(V_{DC} - A)^2\right] \tag{9}$$

where $n = (C_1 + C_2)/C_1$, μ_n is the mobility of electrons in the channel and the capacitance per unit area is denoted by C_{ox}. The MOSFET channel width, length and threshold voltage are expressed as W, L and V_t, respectively. From the Fourier series $I_1(t)$, the fundamental current component is given by

$$I_1(t)|_{fund} \approx \frac{2}{\pi} I_0 \sin(\omega_0 t) \tag{10}$$

and the fundamental voltage amplitude can be expressed as

$$A \approx \frac{2}{\pi} I_0 R_{LM}. \tag{11}$$

From (10) and (11), a simplified expression of the oscillator output voltage is given by

$$V_0 = \frac{V_{DC}}{2\pi}\left(\frac{1}{2} + \frac{C_2}{C_1}\right). \tag{12}$$

D. Modulator

The sensor utilizes the modulated backscattering principle for communication. Modulated backscattering is realized by applying the oscillator output voltage across the rectifier, which is also used as the modulator. The ac output voltage of the oscillator modulates the RF impedance of the rectifier. As a consequence, there are sidebands in the signal reflected from the sensor. Fig. 2 shows the electrical equivalent circuit that is used to derive an equation for the signal reflected from the sensor at one modulation sideband.

Unlike in rectification, non-linear junction capacitance contributes to the mixing due to higher frequencies considered, and it therefore needs to be taken into account. The voltage-dependent junction capacitance of the diode is given as

$$C_{\mathrm{j}}(V_{\mathrm{j}}) = \frac{C_{\mathrm{j0}}}{\left(1 - \frac{V_{\mathrm{j}}}{\Phi}\right)^{\gamma}} \tag{13}$$

where γ is the profile parameter for the depletion capacitance ($\gamma = 0.5$ for a uniformly doped junction), C_{j0} is junction capacitance at zero bias, V_{j} is the voltage across the junction, and Φ is junction potential. The small-signal approximation for the junction currents at zero bias is given as [23]

$$I(V_{\mathrm{j}}) \approx 2\left(\frac{1}{R_{\mathrm{j}}} + \jmath\omega C_{\mathrm{j0}}\right)V_{\mathrm{j}} + \left(\frac{\alpha}{R_{\mathrm{j}}} + \frac{\jmath\omega C_{\mathrm{j0}}\gamma}{\Phi}\right)V_{\mathrm{j}}^2. \tag{14}$$

The first term represents the current of a normal (voltage-independent) capacitor which does not produce any modulated voltages, whereas the second term generates mixing products. Hence, the modulated current (at the first side band) of the equivalent current generator for the Schottky diode is

$$I_{\mathrm{dM}} = 2\sqrt{2P_{\mathrm{in}}R_{\mathrm{a}}}S_{\mathrm{ja}}S_{\mathrm{jm}}V_0\left(\frac{\alpha}{R_{\mathrm{j}}} + \frac{\jmath\omega C_{\mathrm{j0}}}{\Phi}\right) \cdot\left(\cos(\omega_0 - \omega_{\mathrm{osc}})t + \cos(\omega_0 + \omega_{\mathrm{osc}})t\right) \tag{15}$$

where $S_{\mathrm{jm}} = (V_{\mathrm{jm1}} + V_{\mathrm{jm2}})/V_{\mathrm{osc}}$, with V_{jm1} and V_{jm2} being the generated junction voltages due to the oscillator across diodes 1 and 2, respectively. For simplicity, we assume that $V_{\mathrm{jm1}} = V_{\mathrm{jm2}}$. Thus, I_{dM} is the non-linear term of (14). The oscillator output voltage is represented by a voltage source $V_{\mathrm{osc}} = V_0\cos(\omega_{\mathrm{osc}}t)$, where V_0 is the oscillator ac output voltage amplitude and ω_{osc} is oscillator angular frequency. As can be seen from Fig. 2, Z_2 consists of an RF choke and a dc block capacitor. The voltage at $f = f_{\mathrm{RF}} - f_{\mathrm{osc}}$ across the radiation resistance (the backscattered signal at the lower side band) is

$$V_{\mathrm{dM}} = 2\sqrt{2P_{\mathrm{in}}R_{\mathrm{a}}}S_{\mathrm{ja}}S_{\mathrm{jm}}V_0Z_{\mathrm{N}} \cdot\left[\left(\frac{\alpha}{R_{\mathrm{j}}} + \frac{\jmath\omega C_{\mathrm{j0}}}{\Phi}\right)\left(\cos(\omega_0 - \omega_{\mathrm{osc}})t\right)\right] \tag{16}$$

where the impedance of the equivalent Norton current source is Z_{N}, shown in (17), at the top of the next page. The voltage reflected by the antenna can be expressed as

$$V_{\mathrm{ma}} = S_{\mathrm{aM}}V_{\mathrm{dM}} \tag{18}$$

where S_{aM} is the voltage transfer function (equivalent to transmission coefficient S_{21} of a two-port device) between the equivalent source and the antenna.

E. Sensor Response at the Modulation Frequency

By substituting (12) and (16) into (18) we get an equation for the backscattered voltage of the sensor $V_{\mathrm{a,s}}$ (across the antenna) at the lower side band as a function of input power

$$V_{\mathrm{a,s}} = \frac{1}{\pi}\sqrt{2P_{\mathrm{in}}R_{\mathrm{a}}}S_{\mathrm{ja}}S_{\mathrm{jm}}Z_{\mathrm{N}}I_{\mathrm{DC}} \cdot\left[\left(I_{1(\mathrm{j,DC})} + I_{2(\mathrm{j,DC})}\right)\left(\frac{R_{\mathrm{j}}R_{\mathrm{L}}(V_{\mathrm{DC}})}{2R_{\mathrm{j}} + R_{\mathrm{L}}(V_{\mathrm{DC}})}\right)\right] \cdot\left[\left(\frac{1}{2} + \frac{C_2}{C_1 + C_{\mathrm{S}}}\right)\left(\frac{\alpha}{R_{\mathrm{j}}} + \frac{\jmath\omega C_{\mathrm{j0}}}{\Phi}\right)\left(\cos(\omega_0 - \omega_{\mathrm{osc}})t\right)\right] \tag{19}$$

where R_{L} is the input resistance of the oscillator and C_{S} is the capacitance of the sensing element, which in this case is connected parallel to C_1. Moreover, the resistance is assumed constant although in practice it depends on the voltage [33]. This result can be used to describe the backscattered power of the sensor and also to predict the sensor backward read-out distance.

F. Link Budget Calculation for Communication

Let us derive the read-out distance of the sensor. The power received by the sensor located at a distance r from the reader is

$$P_{\mathrm{s}} = P_{\mathrm{t}}G_{\mathrm{r}}G_{\mathrm{s}}\left(\frac{\lambda}{4\pi r}\right)^2 \tag{20}$$

where P_{t} is the power transmitted by the reader, G_{r} is the reader antenna gain (to the direction of the sensor), G_{s} is sensor antenna gain, and λ is the wavelength.

There are two conditions that must be fulfilled in order to read the sensor. First, the sensor must receive enough power to turn on its oscillator. Second, the response signal received by the reader must be above the noise floor of the receiver. These two conditions give two read-out ranges that can be distinct, forward (r_{f}) and backward (r_{b}) read-out ranges. The forward read-out range can be obtained by requiring that the power received by the sensor (as given in (20)) exceeds the threshold power (P_{th}) required to turn on the oscillator. Similarly, the backward read-out range is obtained by requiring that the signal received by the reader is above the noise floor. The read-out distance of the sensor is limited by the smaller one of the forward and backward distances and is given as

$$r = \min_{\substack{P_{\mathrm{th}}=P_{\mathrm{s}}\\ r_{\mathrm{f}}=r_{\mathrm{b}}}}\begin{cases} r_{\mathrm{f}} = \dfrac{\lambda}{4\pi}\sqrt{\dfrac{P_{\mathrm{t}}G_{\mathrm{r}}G_{\mathrm{s}}}{P_{th}}} & \text{(forward)} \\ r_{\mathrm{b}} = \dfrac{\lambda}{4\pi}\sqrt{\dfrac{\Gamma_{\mathrm{m}}P_{\mathrm{th}}G_{\mathrm{r}}G_{\mathrm{s}}}{P_{\mathrm{N}}}} & \text{(backward)} \end{cases} \tag{21}$$

$$Z_{\mathrm{N}} = \frac{1}{j\omega C_{\mathrm{j}} + \frac{1}{R_{\mathrm{j}}} + \frac{1}{\frac{1}{j\omega C_{\mathrm{j}} + \frac{1}{R_{\mathrm{j}}}} + \frac{1}{j\omega C_{\mathrm{p}} + \frac{1}{Z_2}}} + \frac{1}{Z_{\mathrm{a}} + \frac{1}{j\omega C_{\mathrm{b}}}}} \tag{17}$$

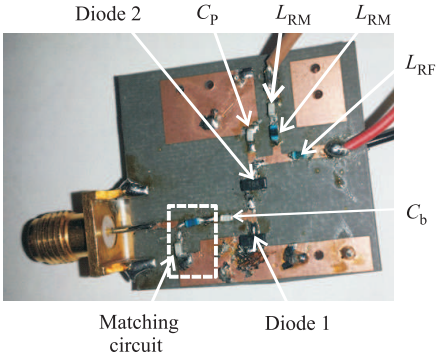

Fig. 5. Photograph of the prototype rectifier and modulator implemented with lumped elements soldered on the PCB.

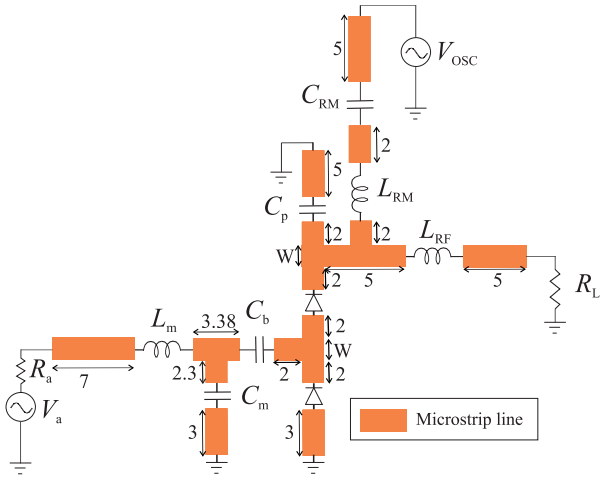

Fig. 6. Schematic circuit of the rectifier and modulator simulation model with microstrip lines. All microstrips have the same width, W = 1 and all dimensions are in millimeters.

where P_{N} is the receiver sensitivity, Γ_{m} is the modulation factor, and r_{f} and r_{b} represents the sensor forward and backward read-out distance, respectively.

III. Experiment and Simulation

UHF RFID frequencies vary in each country depending on particular frequency regulations. The worldwide UHF RFID band is 860−960 MHz. In order to validate the theoretical model in practice, an example sensor design is fabricated and measured. The sensor is designed to operate at 844.5 MHz, and the purpose of the design is to validate the model used rather than to design a sensor for any particular application. Moreover, Schottky diodes are used as rectifier and modulator, and frequency has little influence on their rectification and mixing characteristics. Therefore, our experiment demonstrates the concept also in frequencies allocated to UHF RFID in different countries.

A. Rectifier and Modulator

The rectifier and modulator prototype is implemented with lumped circuit elements soldered on a printed circuit board made from Rogers RT/duroid 5870 substrate ($\varepsilon_r = 2.33, \tan\delta = 0.0012$). Lumped capacitor and inductor are used as matching elements and two zero-bias Schottky diodes as the rectifier and modulator. Fig. 5 shows a photograph of the prototype.

The rectifier and modulator are simulated with ADS (ADS Design Environment, Santa Clara, CA., USA. [Online]. Available: http://www.agilent.com/) using the harmonic balance simulation. Fig. 6 shows the rectifier and modulator simulation model. In simulation, discrete passives are modeled with S-parameters provided by the component manufacturers. The component values used in the calculations, simulations and measurements are listed in Table II.

The rectified voltage is measured with a digital multimeter (HP 3478A) and the modulated voltage at one sideband

TABLE II
Parameters of the Rectifier and Modulator Used in Calculations, Simulations and Measurements

Antenna resistance	$R_{\mathrm{a}} = 50\,\Omega$
Matching inductor	$L_{\mathrm{m}} = 27\,\mathrm{nH}$
RF-block inductor	$L_{\mathrm{RF}} = L_{\mathrm{RM}} = 270\,\mathrm{nH}$
Matching capacitor	$C_{\mathrm{m}} = 6.8\,\mathrm{pF}$
Coupling capacitor	$C_{\mathrm{p}} = 68\,\mathrm{pF}$
Blocking capacitor	$C_{\mathrm{b}} = C_{\mathrm{RM}} = 68\,\mathrm{pF}$
Junction capacitance	$C_{\mathrm{j0}} = 0.18\,\mathrm{pF}$
Saturation current	$I_{\mathrm{s}} = 50\,\mathrm{nA}$
Ideality factor	$n = 1.08$
Series resistance	$R_{\mathrm{s}} = 6\,\Omega$
Junction grading coefficient	$M = 0.5\,\Omega$
Load resistance	$R_{\mathrm{L}} = 0.5\,\mathrm{M}\Omega$
Continuous wave frequency	$f_1 = 844.5\,\mathrm{MHz}$

is measured with a spectrum analyzer (Anritsu MS2683A). A continuous wave (CW) is generated by a signal generator (Rohde & Schwarz SML-03) and fed to the rectifier through a circulator (Voyantic V2.0). For testing purposes, the modulation voltage is generated with a signal generator (Rohde & Schwarz SML-06) at 150 kHz and fed to the oscillation port. The signal reflected from the modulator is distinguished with a circulator and detected by the spectrum analyzer receiver.

The simulated and measured rectified voltage as a function of input frequency is shown in Fig. 7. The input power is kept constant (19 dBm) and the load resistance is 240 kΩ. The simulated and measured curves align almost perfectly at frequencies below 840 MHz, but at higher frequencies the simulated voltage is approximately 10 μV higher than the

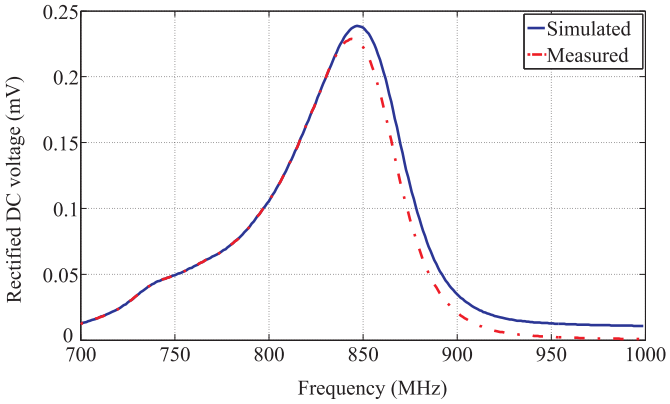

Fig. 7. Rectified DC voltage as a function of frequency. Input power to the rectifier is $P_{in} = -19$ dBm.

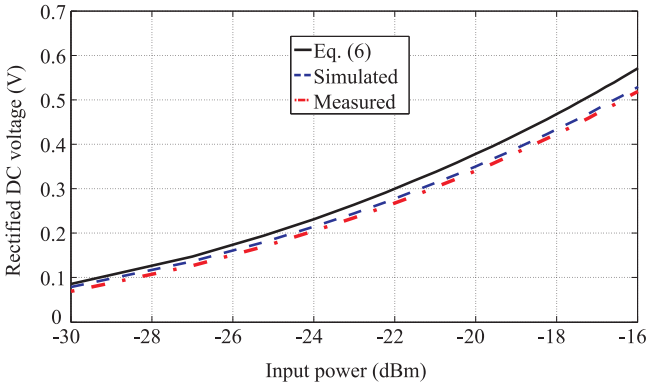

Fig. 8. Rectified DC voltage as a function of input power. The CW frequency is $f_{CW} = 844.5$ MHz.

measured one. The offset between the simulated and measured curves can be caused by, e.g., the accuracy of the printing and etching process, and component variations.

As can be seen in Fig. 7, the circuit exhibits the maximum dc voltage at the input frequency of 844.5 MHz. In general, non-linear properties of diodes change slowly with the frequency, but the peak is due to the matching between the diodes and antenna.

Fig. 8 shows the calculated, simulated, and measured dc voltage of the rectifier at different input power levels. The CW frequency is 844.5 MHz and the output load is $R_L = 0.5\,\mathrm{M}\Omega$, which is the approximate input impedance of the oscillator obtained from the simulation. Fig. 8 exhibits a good agreement between the analytical, simulated and calculated curves at small power levels. The calculated curve would naturally fail at high power levels as the model is derived assuming small-signal analysis.

The backscattered power of the modulator is studied by sweeping the oscillation output voltage and keeping the oscillation frequency and input power constant. Fig. 9 shows the analytical, simulated and measured backscattered power of the modulator as a function of output voltage of the oscillator. The RF input power is -19 dBm and the oscillation frequency is 150 KHz kHz. The simulated and measured curves agree well and they correspond to the analytical results. Note that small deviation in analytical results is due to component losses that

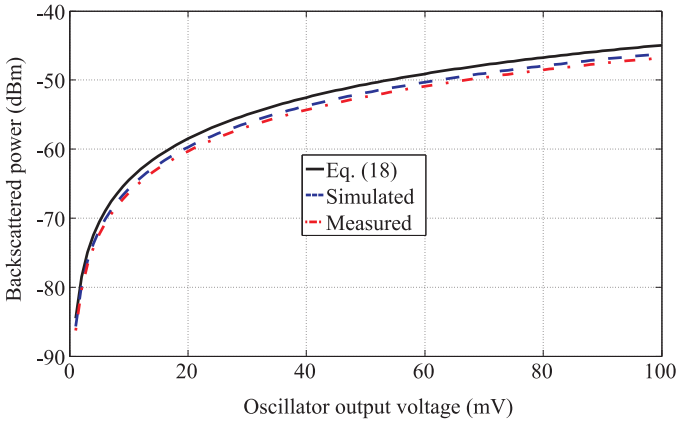

Fig. 9. Backscatter power as a function of oscillator output voltage at input power level of -19 dBm.

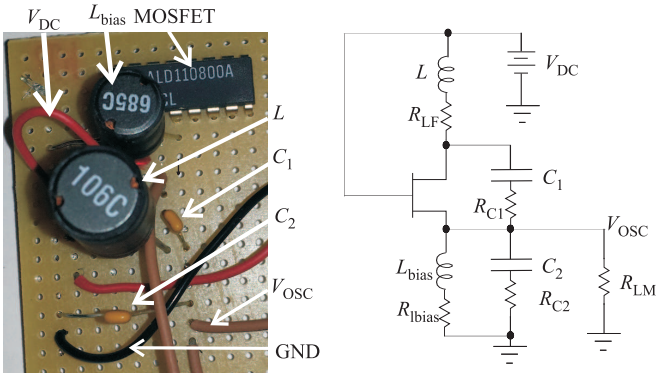

Fig. 10. (a) Photograph of the prototype oscillator implemented by using the BPS stripboard-3u. (b) Schematic circuit of the oscillator simulation model.

are neglected when deriving (18).

B. Oscillator

The oscillator circuit is implemented using the BPS stripboard-3u. An ALD110800A matched pair MOSFET transistor is used in the oscillator, whose prototype is shown in Fig. 10 (a).

Fig. 10 (b) represents a schematic circuit of the oscillator simulation model used in ADS. A SPICE (LEVEL 2) model is used for the transistor in the simulation. The component values used in the simulation, calculation and measurement are listed in Table III.

The oscillator is tested by measuring its output ac voltage and oscillation frequency as a function of input dc voltage supplied by an Agilent E3631A dc voltage supply, and the waveform is captured with an oscilloscope (Tektronix TDS 1002).

The calculated, simulated and measured oscillation frequency as a function of the input dc voltage is shown in Fig. 11. Calculations based on (7) agree well with the simulation, while the measured frequency is approximately 19 % smaller. We assume that the deviation between the measured and simulated curves occurs because of the measurement probe used to measure the oscillation frequency. The probe is a

TABLE III
PARAMETERS OF THE OSCILLATOR USED IN CALCULATIONS, SIMULATIONS AND MEASUREMENTS

Inductor	$L_1 = 10\,\text{mH}$
Series resistance of L_1	$R_{\text{LF}} = 7.3\,\Omega$
Biasing inductor	$L_{\text{bias}} = 6.8\,\text{mH}$
Series resistance of L_{bias}	$R_{\text{L}_{\text{bias}}} = 13.5\,\Omega$
Capacitor	$C_1 = 180\,\text{pF}$
Estimated series resistance of C_1	$R_{\text{C1}} = 136\,\Omega$
Capacitor	$C_2 = 390\,\text{pF}$
Estimated series resistance of C_2	$R_{\text{C2}} = 182\,\Omega$
Load resistance of	$R_{\text{LM}} = 0.5\,\text{M}\Omega$

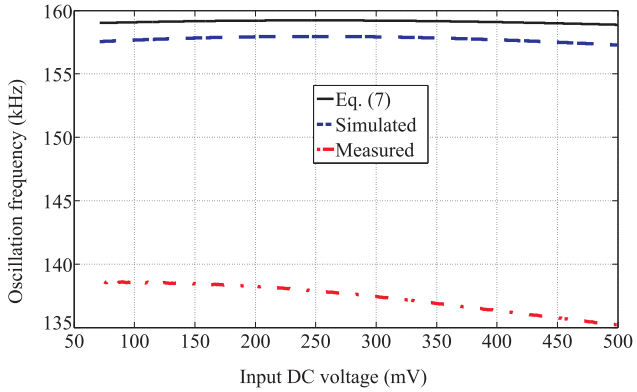

Fig. 11. The measured, simulated and calculated oscillation frequency as a function of input DC supply voltage.

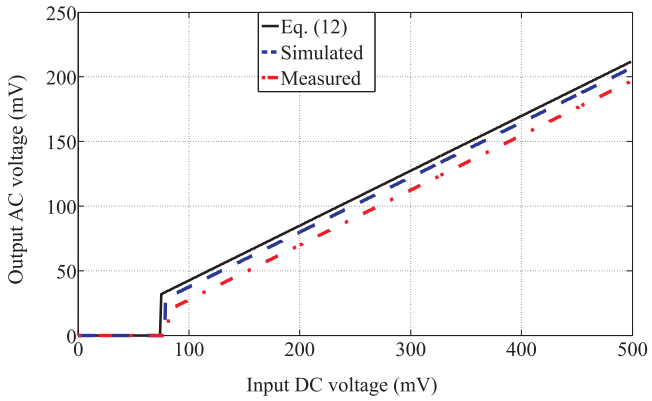

Fig. 12. The measured, simulated and calculated oscillator output voltage as a function of input DC supply voltage.

capacitive load to the oscillator, lowering its frequency. Note that the small deviation between the calculated and simulated frequency is due to parasitic capacitance of the MOSFET. An ideal MOSFET is assumed in the calculated curve.

Fig. 12 shows the measured, simulated, and calculated output voltage of the oscillator at different input dc voltages. According to analytical and simulated results, oscillation is sustained when the input dc voltage is above $69.3\,\text{mV}$ and $73.7\,\text{mV}$, respectively, whereas the measured turn-on voltage is $82.6\,\text{mV}$. Thus, the oscillator turn-on voltage calculated according to (8) corresponds well to the simulated and measured turn-on voltages. Later, oscillator turn-on voltage will

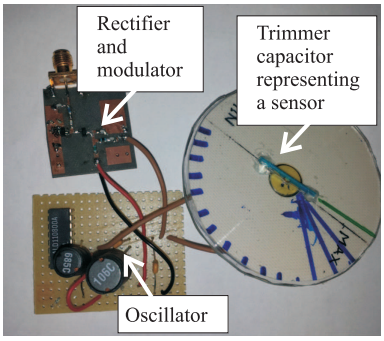

Fig. 13. Photograph of the sensor prototype where a trimmer capacitor is used to represent a sensor.

be considered as the threshold voltage of the sensor.

C. Sensor

The sensor prototype is implemented by integrating all three parts together. A photograph of the sensor prototype is shown in Fig. 13. We demonstrate passive wireless sensor functionality by adding in parallel to capacitor C_1 a trimmer capacitor, to represent a capacitive sensor element. The capacitance of the trimmer capacitor for different rotation angles is measured with an HP 4192A LF impedance analyzer .

In the wired measurement, the CW is generated with a signal generator and fed through a circulator to the sensor, like in the rectifier and modulator measurement. The reflected signal is separated with a circulator and fed to the spectrum analyzer.

In addition to the wired measurement, the sensor response is measured wirelessly. The wireless measurement is carried out with the Voyantic measurement system (Hand carry kit, Voyantic Ltd. [online]. http://www.voyantic.com/) and the sensor is connected to an ultra-wideband patch antenna (FXUB.66 maximus ultra-wide band antenna, Taoglas antenna solution. [Online]. Available: http://www.taoglas.com/). In the measurement, the reader antenna and sensor are placed 8 m away from each other. The Voyantic measurement system was controlled with a LabVIEW-based software.

As can be seen from (19), an analytical equation for the backscattered voltage is derived. However, the sensor read-out distance is always measured from the backscattered power. Thus, the backscattered voltage is converted into backscattered power using the well-known formula $P = V^2/R$. In this case, antenna impedance is matched to $50\,\Omega$. Measured and calculated backscattered power as a function of input power level are shown in Fig. 14. According to the calculation, the threshold power of the sensor is $-28\,\text{dBm}$, whereas it is $-22\,\text{dBm}$ in the measurement. There is an offset between the measured and calculated curves, but they exhibit similar shape. This offset can be due to the input resistance of the oscillator. In the calculation, a $0.5\,\text{M}\Omega$ input resistance was assumed, although it is in reality voltage-dependent and may be different from the assumed value. In addition, the oscillator and modulator input impedances consist of capacitance, inductance and resistance. Complex impedance could be used as a load for better fit.

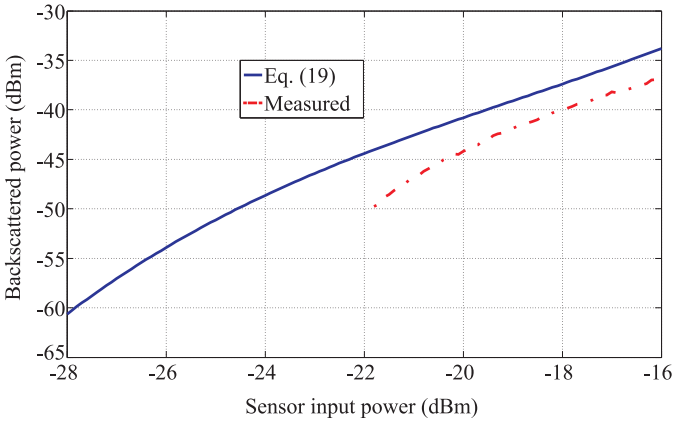

Fig. 14. Backscatter power responses of the sensor as a function of sensor input power levels.

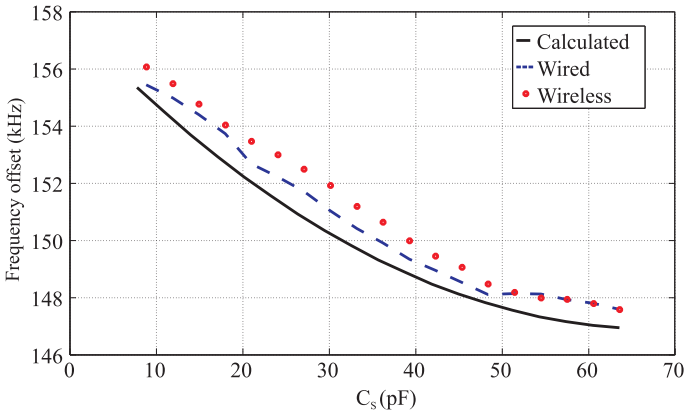

Fig. 15. Sensor oscillation frequencies of the sensor as a function of sensor capacitance.

The wired, wireless and calculated frequency offset is shown in Fig. 15. The slope of the calculated frequency offset slightly differs from the wired and wireless frequency offsets. The deviation is likely caused by the fact that the capacitance value of the trimmer capacitor may change when it is connected to the sensor circuit due to the other sensor components and parasitic effects. Note that the small deviation between wired and wireless measurement is due to the power level received by the sensor. In the wired measurement, the input power level is kept constant at -19 dBm, but in the wireless measurement, power received by the sensor varies due to interference and multipath propagation. In the present case, the corresponding power transmitted by the reader is approximately 27 dBm and the backscattered power received by the reader is -73 dBm. The read-out distance in the wireless experiment was 12 m. The corresponding link budget calculation is presented in Table IV.

Fig. 16 shows the received power in the sensor and in the reader. Sensor sensitivity or power-up threshold of -22 dBm and reader sensitivity of -75 dBm are also shown. In this measurement, sensor response is measured by sweeping the transmitted power of the reader antenna. During the measurement, the sensor is placed 30 cm away from the reader antenna in the anechoic chamber. Finally, sensor forward and

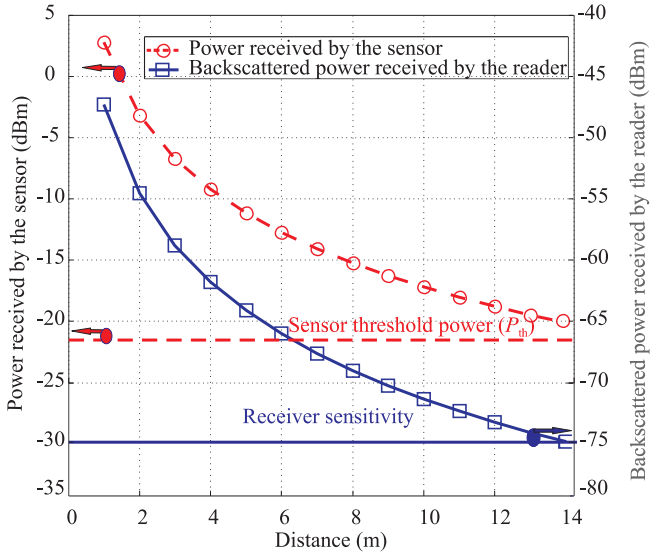

Fig. 16. Measured received power in the sensor and reader as a function of distance. The transmitted power of the reader antenna was 27 dBm.

TABLE IV
THE CALCULATED LINK BUDGET OF A WIRELESS RFID SENSOR INTERROGATED WITH A READER DEVICE ($f = 844.5$ MHz)

Transmitted power	$P_t = 27$ dBm
Reader antenna gain	$G_r = 7.7$ dB
Free space loss ($r = 12$ m)	$\left(\frac{\lambda}{4\pi r}\right)^2 = 52$ dB
Received power by the sensor	-19 dBm
(Threshold power for the sensor	$P_{th} = -22$ dBm)
Modulation loss	8.4 dB
Sensor antenna gain	$G_s = 2.7$ dBi
Received backscatter power by the reader	-73 dBm
(Receiver noise	-75 dBm)

backward read-out distance is calculated accordingly to (21). As can be seen from Fig. 16, when the prototype sensor is interrogated with a reader with 27 dBm transmit power, 7.7 dB antenna gain, and -75 dBm sensitivity, and when the sensor is equipped with an antenna whose gain is 2.7 dBi, the detection distance of the sensor would be 14 m at 844.5 MHz.

IV. CONCLUSION

This paper has discussed an approach that can be used to harness the sensing capabilities of RFID. The presented concept has been analyzed theoretically and verified with simulations and measurements. Moreover, theoretical equations for various properties of the sensor RF parts and oscillator are derived and realized in practice.

A passive wireless sensor using a trimmer capacitor as a sensing element is demonstrated to have a read-out distance of at least 14 m at 844.5 MHz. The experiments demonstrate a very good agreement between the measured and theoretically derived performance of the sensor. The given theoretical models can be applied to predict the sensor performance without carrying out any particular measurements.

Future work includes measuring the oscillator and modulator input impedance for optimizing the sensor performance. In addition, a sensor element will be attached to the oscillator circuit for measuring an external quantity and it will also be integrated into an existing RFID tag in order to enable the features of identification and the possibility to measure an external quantity with larger read-out distance.

REFERENCES

[1] K. Finkenzeller, "RFID Handbook," Munich, John Wiley & Sons Inc., 2003.
[2] A. Rida, L. Yang and M. Tentzeris, "RFID-Enabled Sensor Design and Applications," Artech House, 2010.
[3] R. Want, "Enabling ubiquitous sensing with RFID," *Computer*, vol. 37, no. 4, pp. 84−86, Apr. 2004.
[4] A. P. Sample, D. J. Yeager, P. S. Powledge, A. V. Mamishev, and J. R. Smith, "Design of an RFID-based battery-free programmable sensing platform," *IEEE Trans. Instrum. Meas.*, vol. 57, no. 11, pp. 2608−2615, Nov. 2008.
[5] C. Turcu, Development and Implementation of RFID Technology, InTeh, 2009, pp. 89−178.
[6] A. Vaz, A. Ubarrexena, I. Zalbide, D. Pardo, H. Solar, A. Garcia-Alonso, and R. Berenguer, "Full passive UHF tag with a temperature sensor suitable for human body temperature monitoring," *IEEE Trans. Circuits Syst. II, Exp. Briefs*, vol. 57, no. 2, pp. 95−99, Feb. 2010.
[7] Impinj, Inc., UHF RFID products supplier, Seattle, WA., USA. [Online], Available: http://www.impinj.com/Monza_X_RFID_Chips.aspx (Cited Feb. 03, 2014).
[8] Ams, analog semiconductor manufacturer, Graz, Austria. [Online], Available: http://www.ams.com/eng/Products/UHF-RFID/UHF-Interface-and-SensSe-Tags/SL900A (Cited Feb. 03, 2014).
[9] Farsens, Wireless sensor manufacturer, Donostia-San Sebastian, Spain. [Online], Available: http://www.farsens.com/en/battery-free-sensor-solutions (Cited Feb. 03, 2014).
[10] L. Yang, R. Zhang, D. Staiculescu, C. P. Wong, and M. N. Tentzeris, "A novel conformal RFID-enabled module utilizing inkjet-printed antennas and carbon nanotubes for gas-detection applications," *IEEE Antennas Wireless Propag. Lett.*, vol. 8, pp. 653−656, 2009.
[11] J. Siden, Z. Xuezhi, T. Unander, A. Kotyug, and H.-E. Nilsson, "Remote moisture sensing utilizing ordinary RFID tags," *IEEE Sensors J.*, pp. 308−311, Oct. 2007.
[12] S. Manzari and G. Marrocco, "Modeling and applications of a chemical-loaded UHF RFID sensing antenna with tuning capability," *IEEE Trans. Antennas Propag.*, vol. 62, no. 1, pp. 94−101, Jan. 2014.
[13] S. Rokhsaz and E. de Angle, "Method and apparatus for detecting RF field strength," U.S. Patent 2011/0291810 A1, Dec. 1, 2011.
[14] S. Rokhsaz, "Method and apparatus for varying an impedance," U.S. Patent 2008/0116990 A1, May. 22, 2008.
[15] S. Capdevila, L. Jofre, J. Romeu, and J. C. Bolomey, "Multi-loaded modulated scatterer technique for sensing applications," *IEEE Trans. Instrum. Meas.*, vol. 62, no. 4, pp. 794−805, Apr. 2013.
[16] R. Steindl, A. Pohl, and F. Seifert, "Impedance loaded SAW sensors offer a wide range of measurement opportunities," *IEEE Trans. Microw. Theory Techn.*, vol. 47, no. 12, pp. 2625−2629, Dec. 1999.
[17] A. Pohl, "A review of wireless SAW sensors," *IEEE Trans. Ultrason., Ferroelect., Freq. Control*, vol. 47, no. 2, pp. 317−332, Mar. 2000.
[18] L. Reindl, G. Scholl, T. Ostertag, H. Scherr, U. Wolff, and F. Schmidt, "Theory and application of passive SAW radio transponders as sensors," *IEEE Trans. Ultrason., Ferroelect., Freq. Control*, vol. 45, no. 5, pp. 1281−1292, Sep. 1998.
[19] J. C. Butler, A. J. Vigliotti, F. W. Verdi, and S. M. Walsh, "Wireless, passive, resonant-circuit, inductively coupled, inductive strain sensor," *Sensors and Actuators A: Physical*, vol. 102, no. 1−2, pp. 61−66, Dec. 2002.
[20] J. Voutilainen, Methods and instrumentation for measuring moisture in building structures, D.Sc. dissertation, Dept. of Electrical and Communication Engineering, Helsinki University of Technology, Espoo, Finland, 2005.
[21] S. Saati, R. Varma, M. S. Humayun, and T. Yu-Chong, "Wireless intraocular pressure sensing using microfabricated minimally invasive flexible-coiled LC sensor implant," *J. Microelectromech. Syst.*, vol. 19, no. 4, pp. 721−734, Aug. 2010.
[22] J. Song, V. Viikari, N. Pesonen, I. Marttila, and H. Seppä, "Optimization of wireless sensors based on intermodulation communication," *IEEE Trans. Microw. Theory Tech.*, vol. 61, no. 9, pp. 3446−3452, Sep. 2013.
[23] V. Viikari, J. Song, and H. Seppä, "Passive wireless sensor platform utilizing a mechanical resonator," *IEEE Sensors J.*, vol. 13, no. 4, pp. 1180−1186, Apr. 2013.
[24] V. Viikari, H. Seppä, and D.-W. Kim, "Intermodulation read-out principle for passive wireless sensors," *IEEE Trans. Microw. Theory Techn.*, vol. 59, no. 4, pp. 1025−1031, Apr. 2011.
[25] V. Viikari, H. Seppä, T. Mattila, and A. Alastalo, "Wireless ferroelectric resonating sensor," *IEEE Trans. Ultrason., Ferroelect., Freq. Control*, vol. 57, no. 4, pp. 785−791, Apr. 2010.
[26] V. Viikari and H. Seppä, "RFID MEMS sensor concept based on intermodulation distortion," *IEEE Sensors J.*, vol. 9, no. 12, pp. 1918−1923, Dec. 2009.
[27] C. Hung, V. Landge, S. Thakar, S. Rao, H. Lun-Chen, T. Shou-Jiang, S. Spechler, H. F. Tibbals, and J.-C. Chiao, "Remote detection of gastroesophageal reflux using an impedance and pH sensing transponder," *IEEE MTT-S International Microwave Symposium Digest*, 17-22 June 2012, 3 p.
[28] A. D. DeHennis, and K. D. Wise, "A wireless microsystem for the remote sensing of pressure, temperature, and relative humidity," *J. Microelectromech, Syst.*, vol. 14, no. 1, pp. 12−22, Feb. 2005.
[29] L. Yu-Te, Y. Huanfen, A. Lingley, B. Parviz, and B. P. Otis, "A 3-μW CMOS Glucose Sensor for Wireless Contact-Lens Tear Glucose Monitoring," *IEEE J. Solid-State Circuits*, vol. 47, no.1, pp. 335−344, Jan. 2012.
[30] "Information technology - Radio frequency identification for item management - part 63: Parameters for air interface communication at 860 MHz to 960 MHz Type C ," International standard ISO / IEC 18000-63, 2013.
[31] J. D. Griffin and G. D. Durgin, "Complete link budget for backscatter-radio and RFID system," *IEEE Antennas Propag. Mag.,* vol. 51, no. 2, pp. 11−25, Apr. 2009.
[32] H.-H. Hsieh and L.-H. Lu, "A high-performance CMOS voltage-controlled oscillator for ultra-low-voltage operations," *IEEE Trans. Microw. Theory Techn.*, vol. 55, no. 3, pp. 467−473, Mar. 2007.
[33] Advanced Linear Devices, INC., "ALD110800 Datasheet," [Online]. Available: http://www.aldinc.com/ (Cited Feb. 03, 2014).

Md. Mazidul Islam was born in Rajshahi, Bangladesh, in 1987. He received the Master's degree of radio science and engineering (Tech.) (with distinction) from the Electrical Engineering School, Aalto University, Espoo, Finland, in 2013 and is currently working towards the D.Sc. (Tech.) degree at the same university.

From 2013, he has been with the Department of Radio Science and Engineering, Aalto university School of Electrical Engineering, first as a research assistant and currently as a Research Scientist. His research interests include wireless sensors, RFID, microwave sensor and antennas.

Kimmo Rasilainen was born in Helsinki, Finland, in 1987. He received the B.Sc. (Tech.) and M.Sc. (Tech.) (with distinction) degrees in electrical engineering from Aalto University School of Electrical Engineering, Espoo, Finland, in 2012 and 2013, respectively, and is currently working toward the D.Sc. (Tech.) degree at the same university.

Since 2009, he has been with the Department of Radio Science and Engineering, Aalto University School of Electrical Engineering, first as a Research Assistant and currently as a Research Scientist. His research interests include handset antennas, user effect, bendable antenna structures and wireless sensor applications.

Ville V. Viikari (S'06−A'09−M'09−SM'10) was born in Espoo, Finland, in 1979. He received the Master of Science (Tech.), Licentiate of Science (Tech.) (with distinction), and Doctor of Science (Tech.) (with distinction) degrees in electrical engineering from the Helsinki University of Technology (TKK), Espoo, Finland, in 2004, 2006, and 2007, respectively.

He is currently an Assistant Professor with the Aalto University School of Electrical Engineering, Espoo, Finland. From 2001 to 2007, he was with the Radio Laboratory, TKK, where he studied antenna measurement techniques at submillimeter wavelengths and antenna pattern correction techniques. From 2007 to 2012, he was a Research Scientist and a Senior Scientist with the VTT Technical Research Centre, Espoo, Finland, where his research included wireless sensors, RFID, radar applications, MEMS, and microwave sensors. His current research interests include wireless sensors, RFID, and antennas for mobile networks.

Dr. Viikari has served as the chair of the Technical Program Committee of the 6th ESA Workshop on Millimetre-Wave Technology and Applications and the 4th Global Symposium on Millimeter Waves (GSMM 2011), Espoo, Finland, 2011. He was the recipient of the Young Researcher Award of the Year 2014, presented by the Finnish Foundation for Technology Promotion, IEEE Sensors Council 2010 Early Career Gold Award, the 2008 Young Scientist Award of the URSI XXXI Finnish Convention on Radio Science, Espoo, Finland, and the Best Student Paper Award of the annual symposium of the Antenna Measurement Techniques Association, Newport, RI, USA (October 30−November 4, 2005).